Journal Name

ARTICLE

Probing the Ring-Opening Pathways for Efficient Photocatalytic Toluene Decomposition

Received 00th January 20xx,
Accepted 00th January 20xx

DOI: 10.1039/x0xx00000x

www.rsc.org/

Jieyuan Li,[a, b] Xing'an Dong,[c] Guan Zhang,[d] Wen Cui,[c] Wanglai Cen,[b] Zhongbiao Wu,[e] S. C. Lee,[f] and Fan Dong[a, c*]

The ring-opening process is the rate-determining step for photocatalytic decomposition of aromatic volatile organic compounds (VOCs). However, the ring-opening pathway has not been fully revealed, which renders the efficient photocatalytic VOCs degradation. Taking the photocatalytic toluene degradation as a typical case, the ring-opening pathway and regulation strategy were systematically investigated and proposed in an aim to regulate the rate-determining step and accelerate the reaction rates. Herein, the BiOCl with tailored facets were designed as model photocatalysts to clarify the mechanism of photocatalytic toluene degradation. Theoretical calculations and in situ DRIFTS technology were closely combined to dynamically predict and monitor the photocatalytic toluene degradation reactions. It is revealed that the lowest energy barrier was precisely located at the ring-opening of benzoic acid which was generated from toluene oxidation. This result implied that the benzyl must be fully oxidized to benzoic acid to elevate the ring-opening reaction rates. Moreover, the alternative charge arrangement on the {010} facet of BiOCl facilitated the benzyl oxidation and selectivity for benzoic acid ring-opening reaction, subsequently resulting in the remarkably enhanced photocatalytic efficiency, exceeding that of the {001} facet for by 100% towards toluene decomposition. This work demonstrates that probing and tailoring the ring-opening pathway is vital to increase the overall toluene decomposition efficiency and could provide new insights into the understanding of the photocatalytic reactions in VOCs degradation.

Introduction

As one of the most widespread volatile organic compounds (VOCs) in the atmosphere, toluene contributes to the risk of atmospheric environment and human health significantly.[1-3] The technologies for effective toluene decomposition were thus developed rapidly in the past few decades, mainly including adsorption[4, 5], catalytic combustion[6, 7] and photocatalytic oxidation[8, 9]. Because of the abundant solar energy source and strong oxidation ability, photocatalysis has been widely considered as an efficient approach to remove VOCs for atmospheric environmental remediation.[10-13] Current reports on photocatalytic VOCs degradation are mainly focused on catalysts preparation, modification and performance. The intrinsic relationship between the reaction process and decomposition efficiency has not been well-understood. It is worth noting that even after the complete removal of toluene, many toxic intermediates and byproducts can still be observed.[14, 15] Therefore, the determination of the reaction pathways and rates is vital to evaluate the overall efficiency of photocatalytic toluene decomposition. The dynamic monitoring and regulation of the reaction pathways need to be investigated before the practical application of photocatalytic toluene degradation technology.

In order to realize the complete toluene decomposition, the reaction pathways should be first revealed. General reaction pathways for toluene degradation with •OH radicals are calculated and can be divided into three sections[16-18]: (1) the benzyl oxidation to benzyl alcohol, benzaldehyde and benzoic acid successively (path 1-3); (2) the respective aromatic ring-opening of benzyl alcohol, benzaldehyde and benzoic acid to form a series of hydrocarbon chains (path 4-7); (3) the hydrocarbon chain breakage to generate CO_2 and H_2O for complete toluene decomposition (path 8-11).

Reaction pathways for toluene oxidation induced by •OH radicals:

$$C_7H_8 + {}^{\bullet}OH \rightarrow C_6H_5\text{-}CH_2OH + {}^{*}H \quad (1)$$

$$C_6H_5\text{-}CH_2OH + {}^{\bullet}OH \rightarrow C_6H_5\text{-}CHO + H_2O + {}^{*}H \quad (2)$$

$$C_6H_5\text{-}CHO + {}^{\bullet}OH \rightarrow C_6H_5\text{-}COOH + {}^{*}H \quad (3)$$

$$C_7H_8 + 2{}^{\bullet}OH \rightarrow C_7H_{10}O_2 \quad (4)$$

$$C_6H_5\text{-}CH_2OH + 2{}^{\bullet}OH \rightarrow C_7H_{10}O_3 \quad (5)$$

$$C_6H_5\text{-}CHO + 2{}^{\bullet}OH \rightarrow C_7H_8O_3 \quad (6)$$

[a] Research Center for Environmental Science & Technology, Institute of Fundamental and Frontier Sciences, University of Electronic Science and Technology of China, Chengdu 611731, China.
[b] College of Architecture and Environment, Sichuan University, Chengdu, Sichuan 610065, China.
[c] Chongqing Key Laboratory of Catalysis and New Environmental Materials, College of Environment and Resources, Chongqing Technology and Business University, Chongqing 400067, China.
[d] School of Civil and Environmental Engineering, Harbin Institute of Technology, Shenzhen (HITSZ), Shenzhen 518055, China.
[e] Department of Environmental Engineering, Zhejiang University, Hangzhou 310027, China.
[f] Department of Civil and Environmental Engineering, The Hong Kong Polytechnic University, Hong Kong, P. R. China.
* Email: dfctbu@126.com
Electronic Supplementary Information (ESI) available: See DOI: 10.1039/x0xx00000x

$$C_6H_5\text{-}COOH + 2^{\bullet}OH \rightarrow C_7H_8O_4 \quad (7)$$
$$C_7H_{10}O_2 + 2^{\bullet}OH \rightarrow C_5H_8O_2 + C_2H_4O_2 \quad (8)$$
$$C_7H_{10}O_3 + 2^{\bullet}OH \rightarrow C_5H_8O_3 + C_2H_4O_2 \quad (9)$$
$$C_7H_8O_3 + 2^{\bullet}OH \rightarrow C_5H_6O_3 + C_2H_4O_2 \quad (10)$$
$$C_7H_8O_4 + 2^{\bullet}OH \rightarrow C_5H_6O_3 + C_2H_4O_2 \quad (11)$$

Among these pathways, the ring-opening reactions (path 4-7), which costs high activation energy to proceed, has been regarded as the rate-determining step for overall toluene decomposition.[19-21] In a typical photocatalytic toluene decomposition reaction, semiconductor photocatalysts absorb light to generate separated electrons and holes, which subsequently induce the production of reactive oxygen species (ROS) such as •OH radicals to effectively oxidize the pollutants.[22] Through the attack of •OH radicals on the aromatic ring, the conjugated π system can be broken to realize the ring-opening and subsequent oxidation. However, the ring-opening processes include at least four elementary reactions (path 4-7). Probing the selectivity for ring-opening is thus the key issue to achieve the complete toluene decomposition. This task requires the revealing of the reaction pathways and tailoring of the rate-determining step for smooth ring-opening.

To achieve dynamic tracking of toluene decomposition pathways, the density functional theory (DFT) calculations have been widely recognized as a feasible strategy to simulate and predict the reaction coordinates and activation energy,[23-25] which provide theoretical support for investigating the rate-determining step and regulating the ring-opening process in toluene decomposition. Moreover, the in situ diffused reflectance infrared Fourier transform spectroscopy (DRIFTS) technology, as an effective tool for gas-solid reaction analysis, is applied to monitor the reaction intermediate and unravel the reaction mechanism.[26-28] Sensitive signals can be detected as the reaction time proceeds, which are assigned to the adsorbed pollutants, intermediates and products on the photocatalysts surface. By analyzing and comparing the generation and transformation of these adsorbed species in time sequence, the reaction mechanism of toluene decomposition can be distinctly clarified.

In this work, an attempt was made to closely combine the theoretical and experimental approaches, aiming at dynamically predicting and monitoring the photocatalytic reaction pathways of toluene decomposition on the tailored facets of BiOCl as model photocatalysts. We herein report for the first time that the lowest energy barrier for ring-opening was precisely located at the benzoic acid which was generated from benzyl oxidation. This fact indicates that the benzyl must be fully oxidized to benzoic acid in order to elevate the ring-opening reaction rates. Moreover, it is confirmed by the in situ DRIFTS that the BiOCl photocatalyst with {010} facet exposure showed an enhanced selectivity for ring-opening at benzoic acid. This leads to a smoother ring-opening pathway than that of the {001} facets and facilitates complete toluene degradation. We propose that probing and tailoring the ring-opening pathways is vital to increase the overall toluene decomposition efficiency and provides new insights into the understanding of the photocatalytic reactions in VOCs degradation.

Experimental section

DFT calculations. All the spin-polarized DFT-D2 were carried out in the "Vienna *ab initio* simulation package" (VASP 5.4.1) with the generalized gradient approximation with the Perdew-Burke-Ernzerhof (PBE) exchange and correlation functional.[29, 30] The framework of the projector-augment wave method was considered with the cut-off energy at 450 eV. 5 × 5 × 1 K points were set in the Brillouin zone[31]. The Gaussian smearing width was set to 0.2 eV. The micro-structure of BOC-001 was constructed using a 3 × 3 × 2 supercell with the surface saturated by H atoms, which are in agreement with the published works (Figure S1a in the Supporting Information). A 2 × 3 × 2 supercell was formed for the BOC-010 (Figure S1b). All atoms, except those at the boundary, were allowed to relaxed below 0.02 eV $Å^{-1}$. The adsorption energy (E_{ads}) for reactants and H_2O molecules was calculated with the following equation:

$$E_{ads} = E_{tot} - (E_{mol} + E_{BOC}) \quad (1)$$

where E_{tot}, E_{mol} and E_{BOC} were the total energies of the adsorption structures, the isolated molecules and the BOC-001/BOC-010 structures, respectively.

The nudged elastic band (NEB) code was applied to calculate the reaction coordinates from its initial state (IS) to its final state (FS), which also located the transition state (TS).[32, 33] The activation energy (E_a) and reaction energy (E_r) were calculated to evaluate the difficulty for the reaction to proceed, which were defined as:

$$E_a = E_{TS} - E_{IS} \quad (2)$$
$$E_r = E_{FS} - E_{IS} \quad (3)$$

where E_{IS}, E_{TS} and E_{FS} depicted the total energy of IS, TS and FS, respectively.

Chemicals. All the chemicals were analytically pure without further treatment. $Bi(NO_3)_3{\cdot}5H_2O$(>99.0%), KCl(>99.5%) and NaOH(96%) were all purchased from ChengDu CHRON Chemicals Co,. Ltd. China.

Photocatalysts preparation. BiOCl with tailored facets were fabricated through a reported protocol.[34, 35] In a typical synthesis, 0.97 g of $Bi(NO_3)_3{\cdot}5H_2O$ and 0.15 g of KCl were added to 60 mL deionized water with continuous stirring under the room temperature. 1g NaOH was dissolved into 20 mL deionized water. Then the NaOH solution was dropwise added to the mixture to adjust its pH value to 6.0. After stirring for 30 min, the mixture was moved into a 100 mL Teflon-lined stainless autoclave to complete a hydrothermal process at 160 ℃ for 24 h. After cooling down to room temperature, the resulted precipitates were collected and washed with deionized water and ethanol solution for respective three times. When the mixtures were dried at 60℃, the obtained product was labeled as BOC-010. The product that was without NaOH addition was denoted as BOC-001.

Characterization. The X-ray diffraction (XRD) was measured to investigate the crystal phased of the as-generated samples. The X-ray photoelectron spectroscopy (XPS) was used to study the surface chemical composition. The morphology was investigated via scanning electron microscopy (SEM) and transmission electrons microscopy (TEM). High-resolution TEM (HRTEM) and selected area electron diffraction (SAED) were utilized to verify the exposure of

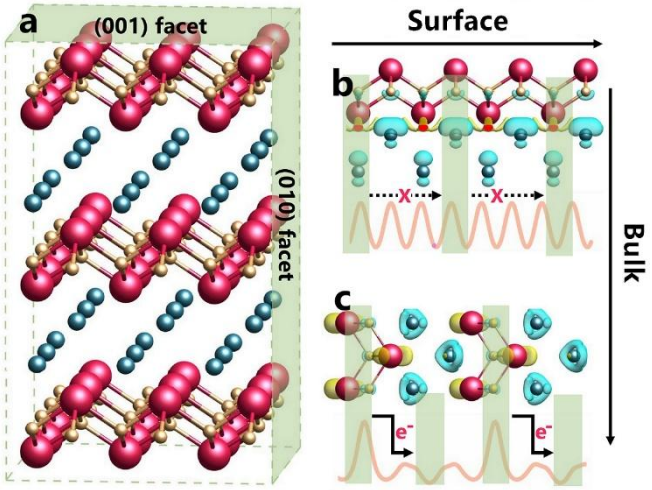

the tailored facets. The UV-vis spectra-photometer was used to characterize the UV-vis diffuse reflectance spectrometry (DRS) spectra. The photoluminescence (PL) spectra of the as-prepared samples were investigated using a fluorescence spectrophotometer.

Figure 1. Charge transfer patterns on the tailored facets of BiOCl: Bulk structure (a); charge difference density distribution on the {001} (b) and {010} (c) facets respectively. The pink lines in (b) and (c) show the electrostatic potential along the surface of {001} and {010} facets respectively. Red, blue and gold spheres depict Bi, Cl and O atoms. The charge accumulation is in blue and depletion is in yellow. The isosurfaces are both set to 0.01 eV $Å^{-3}$ in (b) and (c).

The surface photovoltage (SPV) was measured on the base of the lock-in amplifier and a light chopper. Ns-level time-resolved fluorescence emission spectra were recorded at room temperature with a fluorescence spectrophotometer. Electron spin resonance (ESR) spectra of chemical radicals were obtained to determine the involvement of the ROS under light irradiation.

Photocatalytic degradation of toluene. The photocatalytic efficiency was investigated towards the toluene degradation at 1 L/min in a house-customized continuous flow reaction system (Scheme S1 in the Supporting Information). The as-prepared sample was dispersed on four glass sheets for photocatalytic testing. A UV light source (high-pressure mercury lamp with the maximal radiation wavelength at 365 nm) was vertically placed above the reactor. After the adsorption-desorption equilibrium was achieved, the lamp was turned on. The toluene gas was obtained from a compressed gas cylinder at the concentration of 500 ppm (in N_2) with the flow rate of 100 mL/min. The initial concentration of toluene was diluted to 50 ppm by two separated air flows, respectively wet air at 500 mL/min and dry air at 400 mL/min. The toluene concentration was continuously detected by a gas chromatography (GC 7890 II, Techcomp Co. Ltd.). The toluene removal ratio (η) was calculated as

$$\eta\% = (1 - C/C_0) \times 100\% \quad (4)$$

where C and C_0 depict the toluene concentration in the outlet steam and the feeding stream, respectively.

***In situ* DRIFTS investigation.** *In situ* DRIFTS measurements were performed with a TENSOR II FT-IR spectrometer which was equipped with an *in situ* diffuse-reflectance cell and a reaction chamber, as shown in Scheme S2. High-purity He, high-purity O_2, and 100 ppm of toluene (in He) mixtures were fed into the reaction system, and a tri-way ball valve was used to switch between the target gas (toluene) and purge gas (He). The observation window was made of UV quartz and the IR windows were made of ZnSe. A Xe lamp (MVL-210, Japan) was used as the irradiation light source. Before measurements, prepared samples were pretreated 20 min at 110 °C to removal the adsorbed species on the catalyst surface. The observed absorption bands of the adsorbed species and their chemical assignments are listed in Table S2-S5. The pristine data of DRIFTS was further normalized to investigate the species evolution as time proceeded with a published method.[36]

Results and discussion

Photocatalysts design. BiOCl, with $[Bi_2O_2]^{2+}$ sandwiched in double Cl^- layers, has attracted intensive interest in photocatalysis owning to its fascinating properties on different facets.[37-39] Thus BiOCl was chosen as a model photocatalyst due to the high feasibility to tailor the facets and the distinct atomic exposure on [001] and [010] facets, which helps to investigate the effect of exposed facets on the reaction pathways. The internal electronic field is built by the intrinsic layered structures for charge transfer between $[Bi_2O_2]^{2+}$ and Cl^-. It is worth noting that the charge transfer lengths and directions are quite different on the surfaces of the orthogonal {001} and {010} facets. Hence, distinct photocatalytic efficiency and reaction mechanism are expected on the different facets of BiOCl. As shown in Figure 1a, uniform atomic distribution is observed on the {001} facet (BOC-001), which indicates that the internal electronic field would not be formed along {001} facet. However, as a comparison, the surface atomic alternation of $[Bi_2O_2]^{2+}$ and Cl^- on the {010} facet (BOC-010) should benefit the surface charge transfer because of the built internal electronic field. Detailed analysis of electronic properties is further conducted to verify the charge transfer patterns on different facets. As the charge transfer occurs between $[Bi_2O_2]^{2+}$ and Cl^-, it is proposed by the calculated charge difference density that the charge is transferred along the bulk direction on BOC-001 rather than along the surface (Figure 1b). Furthermore, it is confirmed by the electrostatic potential that the potential barrier on the surface of BOC-001 is difficult for the electrons to overcome, which is not favorable for surface electrons migration. Due to the surface atomic alternation on BOC-010, the potential barrier was significantly decreased in comparison with BOC-001. This could enable the charge transfer along the surface direction from the $[Bi_2O_2]^{2+}$ layer to Cl^- layer (Figure 1c). It is expected that the unique alternative distribution of charge on BOC-010 would contribute to the enhanced charge separation and transformation, subsequently leading to the promotion of pollutants activation and ROS generation for more effective toluene decomposition in comparison with that of BOC-001.

Calculations of the ring-opening pathways for toluene decomposition. In order to elucidate the primary reaction pathways in photocatalytic toluene decomposition, the •OH-driven reaction coordinates were calculated using the NEB method (Figure 2) as the •OH radicals are normally considered as dominant reactive species for photocatalytic oxidation reactions. In order to clearly explain the reaction pathways of toluene oxidation, the water and protons molecules were not shown in Figure 2. The detailed reaction coordinates were listed in the Supporting Information (Figure S2-S4). For the benzyl oxidation part (paths 1-3), no energy barriers are found both on BOC-001 and BOC-010, indicating that toluene can

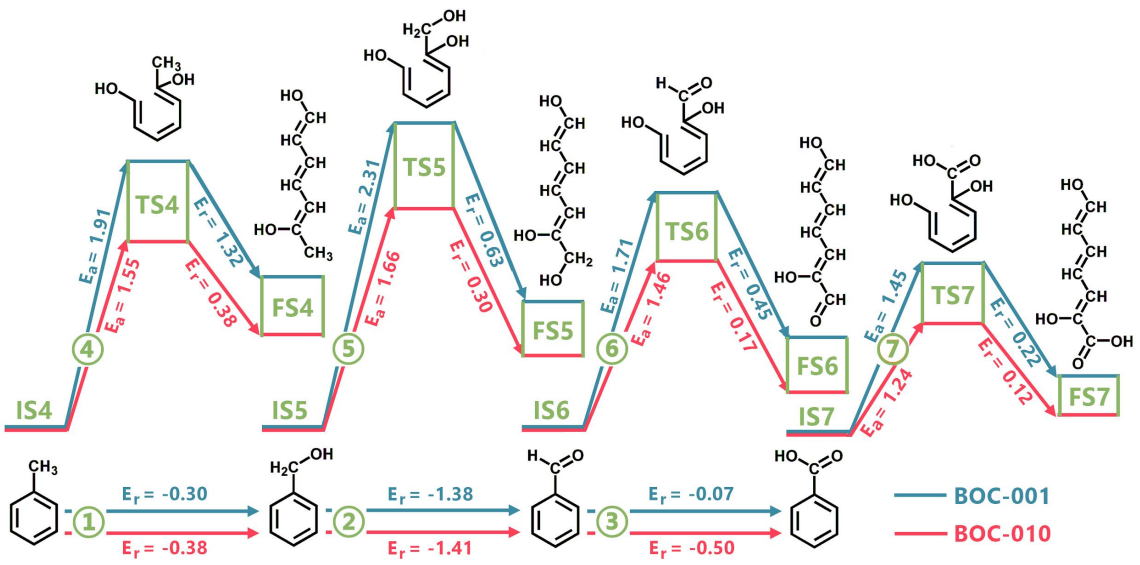

Figure 2. The calculated reaction coordinates for benzyl oxidation (path 1-3) and aromatic ring-opening (path 4-7). The E_a and E_r represent the activation energy and reaction energy respectively (see the experimental section). All the energies are given in eV.

be favorably converted to ring-containing intermediates (benzyl alcohol, benzaldehyde and benzoic acid). However, for full mineralization of toluene, the benzene ring in these intermediates requires to be opened. As can be seen in paths 4-7 in Figure 2, if the ring-opening reaction directly proceeds on toluene (path 4), the activation energies are as high as 1.91 eV in BOC-001 and 1.55 eV in BOC-010. Fortunately, low activation energies are required for the ring-opening reactions at benzaldehyde and benzoic acid. Especially, the lowest energy barrier is located for the ring-opening starting from benzoic acid. These results indicate that more efficient ring-opening reaction can be realized as the benzyl becomes fully oxidized. In addition, the reaction coordinates for carbon chain breakage are subsequently calculated (Figure S4), which implies that the chain breakage reaction needs no energy barriers and these reactions were energy-favorable. Thus, the carbon chain from the ring-opening should be readily degraded into final products.

These theoretical results clearly demonstrate that the ring-opening reaction plays a key role in determining the overall decomposition efficiency, which can be significantly enhanced if the benzyl gets fully oxidized to benzoic acid. It is also certified that the energy barrier for benzoic acid decomposition can be further decreased on BOC-010 via the particular alternative charge distribution in comparison with BOC-001. Thus, the {010} facet could provide active centers for efficient charge transfer, pollutants activation and ROS generation. By the rational facet regulation of BiOCl, it is expected that the ring-opening pathways of photocatalytic toluene decomposition can be tailored for efficient overall toluene degradation.

Photocatalysts fabrication and characterizations. To experimentally support the perspective predicted by DFT calculations, the BiOCl photocatalysts were fabricated with {001} and {010} facets exposure. The morphology of the as-prepared samples was revealed by SEM and TEM examination. The results indicate that both BOC-001 (Figure 3a and S5a) and BOC-010 (Figure 3b and Figure S5b) consist of nanosheet-shaped structures with thicknesses of *ca.* 100 nm. The lattice fringes with a spacing of 0.28 nm are observed in the HRTEM of BOC-001 (Figure 3c), which can be indexed as the (110) atomic plane.[34, 40] Besides, The observed 45° in the SAED pattern agrees with the theoretical value of the angle between the (200) and (110) planes. Based on these results, the BOC-001 samples are identified as the {001} facet exposure.[41] Moreover, the typical TEM image of BOC-010 (Figure 3d) reveal the lattice fringes of 0.37 nm in the (002) plane. It is also confirmed that the interfacial angle of (002) and (102) planes is 43.4°. These results demonstrate that BOC-010 is enclosed by the {010} facet. As evidenced by the HRTEM and SAED results, it can be concluded that the BiOCl photocatalysts with tailored {010} and {001} facets have been successfully fabricated.

As suggested by the XRD patterns (Figure 3e), the intensity ratio of (101) and (102) peaks are significantly different between BOC-001 and BOC-010. The diverse intensity ratios indicate the different direction of crystal growth on these two samples, which were in accordance with the HRTEM and SAED results.[34, 42]. The XPS spectra (Figure S6) indicate that the O atomic amount is decreased while the Bi and Cl atomic amounts are increased in BOC-010 in comparison with that of BOC-001. This result confirms the uniform O exposure on the surface of BOC-001 and alternative exposure of $[Bi_2O_2]^{2+}$ and Cl^- on the surface of BOC-010, which are in accordance with the theoretical simulation results (Figure S1).

The PL and SPV spectra were performed to investigate the charge separation and transformation properties (Figure 3f). Both the BOC-010 and BOC-001 samples display emission peaks in the range of 300-450 nm. Obviously, the lower PL intensity and stronger SPV intensity of BOC-010 than that of BOC-001 can be observed, which indicate the enhanced charge separation capacity. This observation can be explained by the fact that the alternative atomic distribution on the surface of BOC-010 could promote the electrons mobility (Figure 1c). The time-resolved fluorescence decay spectra were utilized to further testify the charge motion dynamics (Figure 3g). In contrast to BOC-001, the lifetime of charge carriers on BOC-010 are clearly prolonged, which further confirm that the alternative atomic distribution could effectively boost the charge separation and transfer. Besides, the ESR spectra were performed with TEMPO as the electrons capture agent (Figure 3h). Three signal peaks can be

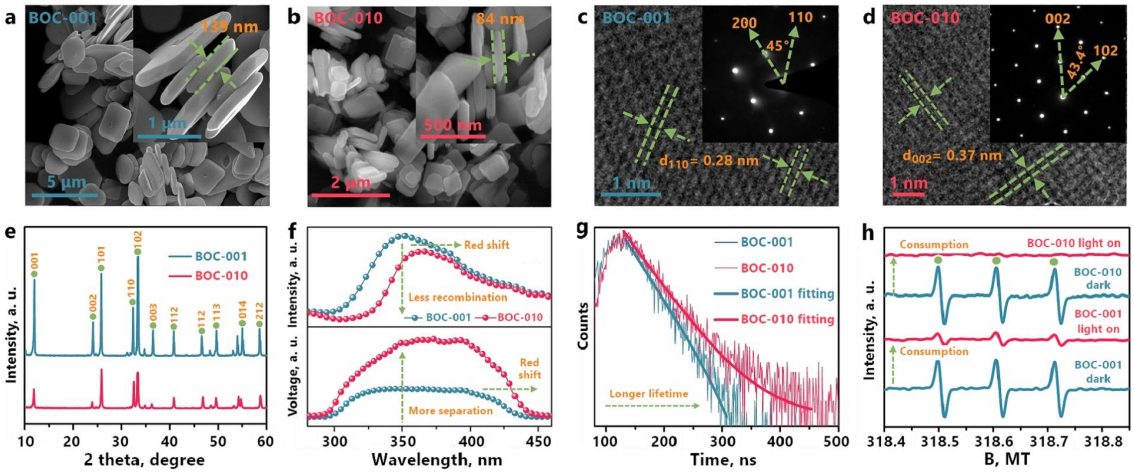

Figure 3. Photocatalysts characterizations: SEM images for BOC-001 (a) and BOC-010 (b); HR-TEM and SAED for BOC-001 (c) and BOC-010 (d); XRD patterns (e); PL (up) and SPV (down) spectra (f); ns-level time-resolved fluorescence spectra (g); ESR spectra for TEMPO photo-excited electrons (h).

detected in dark for both BOC-001 and BOC-010. When TEMPO is irradiated, the distinct decrease of the signals is observed, suggesting that the TEMPO is consumed by photo-excited electrons.[43] It is found that more amount of TEMPO is consumed on BOC-010 than BOC-001, which implies that more photo-excited electrons were generated on BOC-010 under light irradiation due to the enhanced charge separation efficiency. These photoelectrical properties clearly demonstrate that {010} facet of BiOCl is efficient in charge carrier separation and transportation. As a result, BOC-010 is expected to exhibit superior photocatalytic activity than BOC-001.

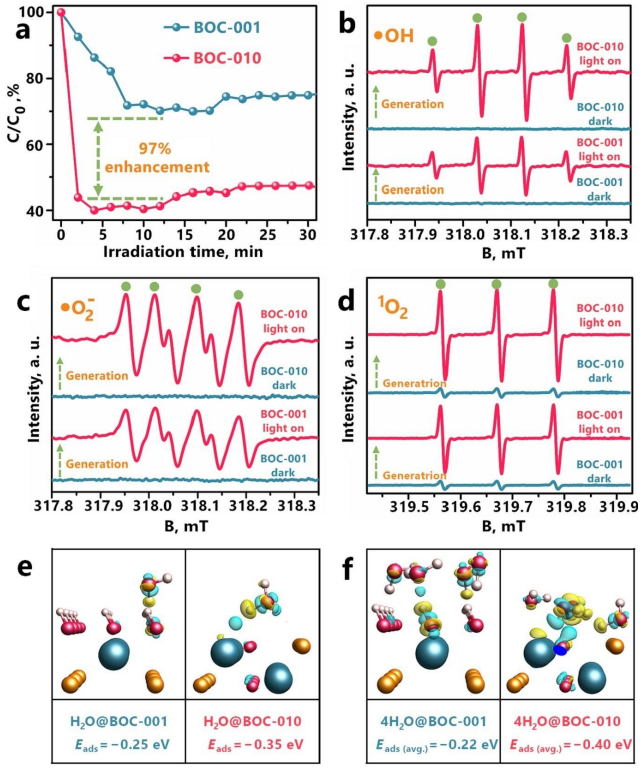

Figure 4. Photocatalytic toluene degradation efficiency and ROS generation: Photocatalytic efficiency evaluation towards toluene degradation under UV-light; ESR for DMPO-•OH (b), DMPO-$•O_2^-$ (c) and TEMP-$^1O_2$ (d); Calculated one and four H_2O molecules adsorption and activation for •OH generation on BOC-001 (e) and BOC-010 (f) respectively. Blue, yellow, red and pink spheres depict Bi, Cl, O and H atoms correspondingly. Charge accumulation is in blue and depletion is in yellow. The isosurfaces are set to 0.0015 eV Å^{-3}.

Photocatalytic toluene decomposition and ROS generation. The photocatalytic performance of the as-prepared samples was investigated towards decomposition of toluene in air under UV light , using a house-customized continuous flow reaction system (Scheme S1). As Figure 4a represented, the maximum toluene purification was obtained at *ca.* 10 min on both catalysts. More importantly, BOC-010 displays a much higher toluene removal ratio (61.0%) than that of BOC-001 (31.0%). We conducted extra photocatalytic efficiency tests of BiOCl towards the degradation of gaseous benzene and dimethylbenzene (Figure S7), these results indicated that BOC-010 also possesses higher efficiency towards the degradation of other aromatic VOCs. Typically, the photocatalytic performance is closely related with the ROS generation. The ESR spectra were then performed to identify the ROS generation during the photocatalytic reaction, including DMPO-•OH (Figure 4b), DMPO-$•O_2^-$ (Figure 4c) and TEMP-$^1O_2$ (Figure 4d).[44] Compared with BOC-001, the signal intensities on BOC-010 are all much stronger for •OH, $•O_2^-$ and $^1O_2$ radicals. The increased ROS generation is beneficial to elevate the oxidation capacity.

Based on the results of the UV-vis DRS (Figure S8) and UPS results (Figure S9), The band structure in conjunction with potentials for radicals formation is illustrated in Figure S10. It is found that the potential energy of the valance band (VB) holes is positive enough to directly oxidize H_2O/OH^- into •OH radicals, which dominantly contributes to the decomposition of toluene. However, the potential energy of the conduction band (CB) electrons is not negative to reduce O_2 molecules. Thus the generation of $•O_2^-$ and $^1O_2$ should originate from the primary •OH on the VB along the path of $H_2O/OH^- \rightarrow$ •OH $\rightarrow H_2O_2 \rightarrow •O_2^- \rightarrow {}^1O_2$ (path S1-S4 in Figure S10)[45-47] The increased •OH generation on BOC-010 is further confirmed by DFT calculations in terms of H_2O activation. In comparison with BOC-001 (Figure 4e and Figure S11a-11d), more intense charge transfer between H_2O molecules and BOC-010 can be observed (Figure 4f and Figure S11e-11h), which leads to the increased E_{ads} of all the calculations including one to four H_2O molecules adsorption. The theoretical simulation implies that the H_2O molecules activation on {010} facet is greatly facilitated, which

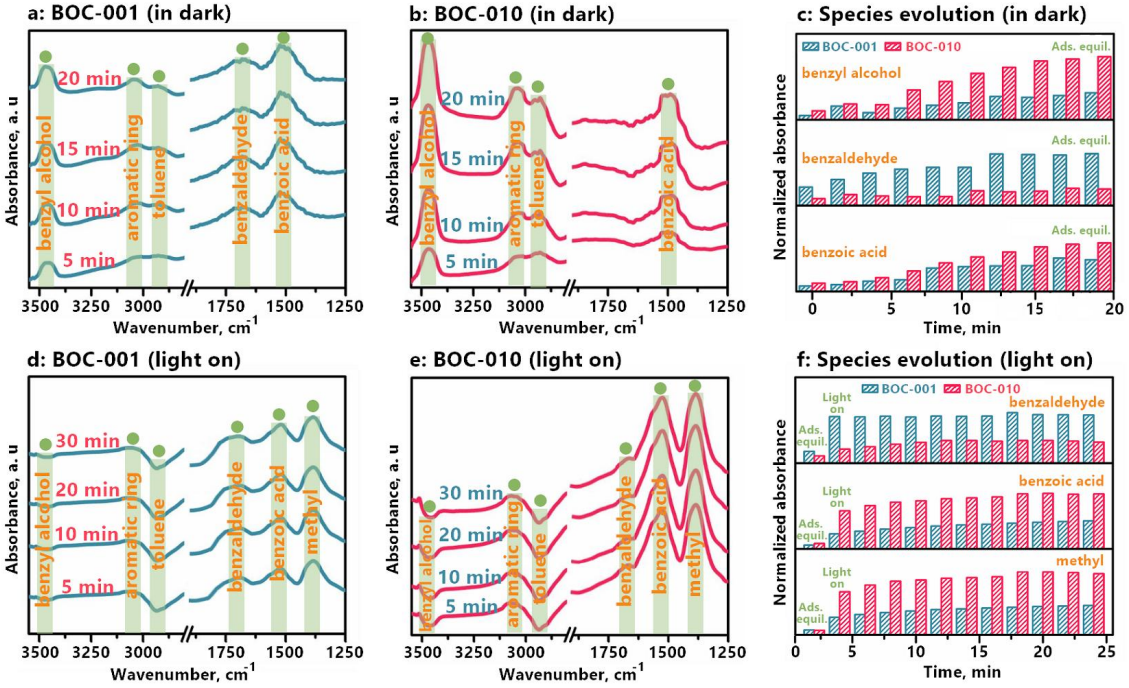

Figure 5. Determination of reaction intermediates and products: *in situ* DRIFTS spectra and species evolution of toluene adsorption in dark (a-c) and oxidation under light irradiation (d-f) on BOC-001 and BOC-010. The range of y-axis is set consistently respectively for the spectra in dark and with light on. The intensity of baselines is deducted in (a) and (b), and the intensity of adsorption equilibrium lines is deducted in (d) and (e).

can be attributed to the atomic alternation on the {010} surface. The highly enhanced H_2O molecules activation could promote more efficient generation of •OH radicals than that on BOC-001 via the H_2O oxidation by the photogenerated holes.

Reaction intermediates and mechanism. In order to confirm the theoretical predication and establish a panoramic understanding of how the BiOCl facets tune the reaction pathways, the *in situ* DRIFTS was employed to dynamically track the primary reaction intermediates and products during the toluene decomposition reaction. It can be observed that the typical DRIFTS absorption peak of toluene (2924 cm^{-1} for BOC-001) is detected immediately after the injection of the gases in the dark condition (Figure 5a).[4]8 As the adsorption is proceeded, increased accumulation of the intermediates including benzyl alcohol (3469 cm^{-}),[49,50] benzaldehyde (1699 cm^{-})[17, 48-50] and benzoic acid (1509 cm^{-})[17, 48, 4]9 are found, which indicates that the toluene conversion can take place at the ambient condition without light irradiation. This result is consistent with our theoretical calculations that the benzyl oxidation consisted of three energy-favorable reactions (paths 1-3 in Figure 1 and S2). As for BOC-010 (Figure 5b), the peaks of toluene (2926 cm^{-}), benzyl alcohol (3469 cm^{-}) and benzoic acid (1509 cm^{-}) can also be observed, similar to that of BOC-001. However, it is notable that benzaldehyde is barely detected for BOC-010. As the results of normalized species evolution (Figure 5c) suggest, the accumulated amount of benzyl alcohol and benzoic acid of BOC-010 is significantly higher than of BOC-001, while the accumulation of benzaldehyde manifests the opposite trend.

After the adsorption equilibrium is reached at 20 min, the DRIFTS are continuously recorded with light irradiation to explore the photocatalytic toluene decomposition mechanism, especially for the ring-opening process. As shown in Figure 5d, the peak intensities of toluene and benzyl alcohol on BOC-001 are gradually decreased and converted to benzaldehyde and benzoic acid. Notably, a new emerging peak at 1383 cm^{-1} is evidently detected under light irradiation, which was assigned to C-H bending vibration in methyl.[48, 51] This peak can be regarded as the principal intermediates after the photocatalytic ring-opening reaction.[50, 51] This result certifies that the BiOCl photocatalyst is sensitive to light and can effectively catalyze the toluene oxidation reaction. These C-H containing intermediates after ring-opening can be readily degraded to generate CO_2 and H_2O based on our theoretical calculations (paths 8-11 in Figure S4). Thus, it is reasonable that no other chain hydrocarbons are detected on the catalyst surface. Similar phenomena are also observed in BOC-010 (Figure 5e). It is important to note that the DRIFTS intensities of benzoic acid and methyl are much higher than that of BOC-001. To be more specific, the normalized species evolution (Figure 5f) implies that the accumulated amount of benzoic acid is increased on BOC-010, in accordance with the theoretical calculation results (paths 4-7 in Figure 1 and S3) that more effective ring-opening reaction can take place starting at benzoic acid. Benzoic acid is decomposed to generate methyl intermediates and subsequent final products for the over-all degradation of toluene.

After a comprehensive comparison of the DRIFTS results between BOC-001 and BOC-010, it can be found that the selectivity for ring-opening reaction is realized on BOC-010. That is, the ring-opening is selectively started benzoic acid, which could promote full toluene oxidation. However, much more benzaldehyde is accumulated on BOC-001, leading to higher E_a for ring-opening at benzaldehyde (path 6 in Figure 1) than that of benzoic acid (path 7 in Figure 1). Combining the theoretical and experimental results, it is clarified that benzyl requires to be fully oxidized to form benzoic acid, which would subsequently contribute to a smooth ring-opening reaction and effective over-all toluene decomposition.

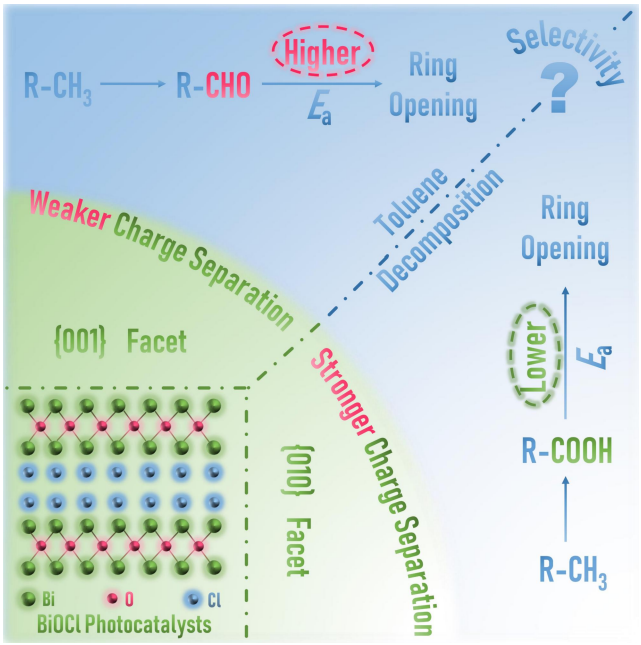

Figure 6. The illustration of the new concept for the understanding the facets-mediated ring-opening pathways.

The underlying mechanism for the difference of reaction selectivity between BOC-001 and BOC-010 is then revealed by DFT calculations (Figure S12). It is found that the E_{ads} is increased on BOC-010 for the adsorption of these aromatic-ring containing species than that of BOC-001, which suggests that the promoted charge transfer between the absorbents and BOC-010 would contribute to the benzyl oxidation. Especially, the patterns of E_{ads} for benzaldehyde and benzoic acid between BOC-001 and BOC-010 are inverse, which may indicate that benzaldehyde is more favorable to be converted on BOC-001, while benzoic acid would be decomposed more easily
on BOC-010 to realize smoother ring-opening reactions. The diverse selectivity for ring-opening reaction on different facets is further confirmed by the calculated projected density of states (PDOS, Figure S13) for C 2p in different benzene series. It can be concluded that the gap energy (E_g) manifests the pattern of benzaldehyde (2.93 eV) < benzoic acid (4.05 eV) < toluene (4.92 eV) < benzyl alcohol (5.00 eV) on BOC-001 and benzoic acid (3.40 eV) < benzaldehyde (3.80 eV) < toluene (4.64 eV) < benzyl alcohol (4.88 eV) on BOC-010. The E_g determines difficulty for electrons hopping from valence band maximum to its conduction band minimum, which results in smoother conversion of benzaldehyde on BOC-001 and benzoic acid on BOC-010. That is, the selectivity for ring-opening reaction is located at benzoic on BOC-010, leading to enhanced photocatalytic efficiency than that of BOC-001.

Conclusions

The concept of the present work is illustrated in Figure 6, which would exert significant implications for future work. On one hand, the reactants activation and ROS generation are significantly enhanced owing to the alternative charge arrangement on the {010} facet. On the other hand, the ring-opening process as the rate-determining step can be tailored by the specific facets. By utilizing the facets tailoring strategy on BiOCl, the selective ring-opening at benzoic acid has been realized. The closely combined theoretical and experimental method proposed in this work provided an effective approach to probe the ring-opening pathways for efficient toluene decomposition, which can be taken as a typical case study in wide applications of photocatalysis in environmental and energy related applications.

Conflicts of interest

There are no conflicts to declare in this work.

Acknowledgements

This work was supported by the National Key R&D Plan (2016YFC02047), the National Natural Science Foundation of China (21822601, 21777011 and 21501016), the Innovative Research Team of Chongqing (CXTDG201602014), the Key Natural Science Foundation of Chongqing (cstc2017jcyjBX0052), the Plan for "National Youth Talents" of the Organization Department of the Central Committee, the Youth Project in Science and Technology Innovation Program of Sichuan Province (17-YCG053) and Graduate Student's Research and Innovation Fund of Sichuan University (2018YJSY011). The authors also acknowledge the AM-HPC in Suzhou, China for computational support.

References

1. M. Muñoz-Batista, A. Kubacka and M. Fernandez-Garcia, *ACS Catal.*, 2014, 4, 4277-4288.
2. S. Weon and W. Choi, *Environ. Sci. Technol.*, 2016, 50, 2556-2563.
3. Y. Ji, J. Zhao, H. Terazono, K. Misawa, N. P. Levitt, Y. Li, Y. Lin, J. Peng, Y. Wang, L. Duan, B. Pan, F. Zhang, X. Feng, T. An, W. Marrero-Ortiz, J. Secrest, A. Zhang, K. Shibuya, M. Molina and R. Zhang, *Proc. Natl. Acad. Sci. U. S. A.*, 2017, 114, 8169-8174.
4. P. Lazar, F. Karlický, P. Jurečka, M. Kocman, E. Otyepková, K. Šafářová and M. Otyepka, *J. Am. Chem. Soc.*, 2013, 135, 6372-6377.
5. R. Slioor, J. Kanervo, T. Keskitalo and A. O. Krause, *Appl. Catal. A: Gen.*, 2008, 344, 183-190.
6. F. Wang, H. Dai, J. Deng, G. Bai, K. Ji and Y. Liu, *Environ. Sci. Technol.*, 2012, 46, 4034-4041.
7. W. B. Li, J. X. Wang and H. Gong, *Catal. Today*, 2009, 148, 81-87.
8. V. Héquet, C. Raillard, O. Debono, F. Thévenet, N. Locoge and L. L. Coq, *Appl. Catal. B: Environ.*, 2018, 226, 473-486.
9. Y. Xu, W. Wen and J. M. Wu, *J. Hazard. Mater.*, 2017, 343, 285.
10. S. Chen, H. Wang, M. Shi, H. Ye and Z. Wu, *Environ. Sci. Technol.*, 2018, 52, 8568-8577.
11. S. Sahu, M. Qanbarzadeh, M. Ateia, H. Torkzadeh, A. Maroli and E. Cates, *Environ. Sci. Technol. Lett.*, 2018, 5, 533-538.
12. D. Liu, J. Wang, X. Bai, R. Zong and Y. Zhu, *Adv. Mater.*, 2016, 28, 7284-7290.
13. Q. M. Ren, S. P. Mo, R. S. Peng, Z. T. Feng, M. Y. Zhang, L. M. Chen, M. L. Fu, J. L. Wu and D. Q. Ye, *J. Mater. Chem. A*, 2018, 6, 498-509.
14. H. Y. Ma, L. Zhao, D. B. Wang, H. Zhang and L. H. Guo, *Environ. Sci. Technol.*, 2018, 52, 2870-2877.
15. P. K. Hong and Y. Zeng, *Water Res.*, 2002, 36, 4243-4254.
16. A. J. Maira, J. M. Coronado, V. Augugliaro, K. L. Yeung, J. C. Conesa and J. Soria, *J. Catal.*, 2001, 202, 413-420.
17. Y. He, Z. Rui and H. Ji, *Catal. Commun.*, 2011, 14, 77-81.
18. M. Wang, F. Zhang, X. Zhu, Z. Qi, B. Hong, J. Ding, J. Bao, S. Sun and C. Gao, *Langmuir*, 2015, 31, 1730-1736.
19. O. Fontellescarceller, M. J. Muñozbatista, M. Fernandezgarcia and A. Kubacka, *ACS Appl. Mater. Interfaces*, 2016, 8, 2617-2627.

20. H. Li, R. Liu, S. Lian, Y. Liu, H. Huang and Z. Kang, *Nanoscale*, 2013, 5, 3289-3297.
21. F. Zhang, M. Wang, X. Zhu, B. Hong, W. Wang, Z. Qi, W. Xie, J. Ding, J. Bao and S. Sun, *Appl. Catal. B: Environ.*, 2015, 170-171, 215-224.
22. Y. Nosaka and A. Y. Nosaka, *Chem. Rev.*, 2017, 117, 11302-11336.
23. J. Li, S. Yin, F. Dong, W. Cen and Y. Chu, *ACS Appl. Mater. Interfaces*, 2017, 9, 19861-19869.
24. J. Li, X. Dong, Y. Sun, G. Jiang, Y. Chu, S. Lee and F. Dong, *Appl. Catal. B: Environ.*, 2018, 239, 187-195.
25. G. Gao, Y. Jiao, E. Waclawik and A. Du, *J. Am. Chem. Soc.*, 2016, 138, 6292-6297.
26. W. Cui, J. Li, F. Dong, Y. Sun, G. Jiang, W. Cen, S. C. Lee and Z. Wu, *Environ. Sci. Technol.*, 2017, 38, 10746-10753.
27. J. Li, Z. Zhang, W. Cui, H. Wang, W. Cen, G. Johnson, G. Jiang, S. Zhang and F. Dong, *ACS Catal.*, 2018, DOI: 10.1021/acscatal.1028b02459.
28. H. Sheng, M. Oh, W. Osowiecki, W. Kim, A. Alivisatos and H. Frei, *J. Am. Chem. Soc.*, 2018, 140, 4363-4371.
29. G. Kresse and J. Furthmüller, *Phys. Rev. B*, 1996, 54, 11169-11186.
30. J. Perdew, K. Burke and M. Ernzerhof, *Phys. Rev. Lett.*, 1996, 77, 3865-3868.
31. G. Kresse and J. Furthmüller, *Comp. Mater. Sci.*, 1996, 6, 15-50.
32. G. Henkelman and H. Jónsson, *J. Chem. Phys.*, 2015, 113, 9978-9985.
33. G. Henkelman, *J. Chem. Phys.*, 2000, 113, 9901-9904.
34. J. Jiang, K. Zhao, X. Xiao and L. Zhang, *J. Am. Chem. Soc.*, 2012, 134, 4473-4476.
35. F. Dong, T. Xiong, S. Yan, H. Wang, Y. Sun, Y. Zhang, H. Huang and Z. Wu, *J. Catal.*, 2016, 344, 401-410.
36. L. Sivachandiran, F. Thevenet, A. Rousseau and D. Bianchi, *Appl. Catal. B: Environ.*, 2016, 198, 411-419.
37. Q. Li, X. Zhao, J. Yang, C. J. Jia, Z. Jin and W. Fan, *Nanoscale*, 2015, 7, 18971-18983.
38. J. Li, H. Li, G. Zhan and L. Zhang, *Acc. Chem. Res.*, 2016, 50, 112.
39. X. Wu, H. Yun, L. Wang, Y. Du, S. Dou, R. Amal and J. Scott, *J. Mater. Chem. A*, 2017, 8117-8124.
40. H. Lin, L. Ding, Z. Pei, Y. Zhou, J. Long, W. Deng and X. Wang, *Appl. Catal. B: Environ.*, 2014, 160, 98-105.
41. L. Sun, L. Xiang, X. Zhao, C. Jia, J. Yang, Z. Jin, X. Cheng and W. Fan, *ACS Catal.*, 2015, 5, 3540-3551.
42. J. Li, K. Zhao, Y. Yu and L. Zhang, *Adv. Func. Mater.*, 2015, 25, 2189-2201.
43. M. Chen, Y. Li, Z. Wang, Y. Gao, Y. Huang, J. Cao, W. Ho and S. Lee, *Ind. Eng. Chem. Res.*, 2017, 56.
44. R. Floyd and L. Soong, *Biochem. Biophys. Res. Commun.*, 1977, 74, 79-84.
45. S. Banerjee, S. Pillai, P. Falaras, K. O'Shea, J. Byrne and D. Dionysiou, *J. Phys. Chem. Lett.*, 2014, 5, 2543-2554.
46. J. Xiao, J. Rabeah, J. Yang, Y. Xie, H. Cao and A. Brückner, *ACS Catal.*, 2017, 7, 6198-6206.
47. R. X. Qu, W. F. Zhang, X. Y. Liu, Y. N. Liu, T. Shih, Y. Wei and L. Feng, *J. Mater. Chem. A*, 2018, 6, 18003-18009.
48. S. Besselmann, E. Löffler and M. Muhler, *J. Mole. Catal. A.*, 2000, 162, 401-411.
49. J. Li, H. Na, X. Zeng, T. Zhu and Z. Liu, *Appl. Surf. Sci.*, 2014, 311, 690-696.
50. Y. Irokawa, T. Morikawa, K. Aoki, S. Kosaka, T. Ohwaki and Y. Taga, *Phys. Chem. Chem. Phys.*, 2006, 8, 1116-1121.
51. W. Simons, *The Sadtler handbook of infrared spectra*, Sadtler Research Laboratories, 1978.

